Computers and Mathematics with Applications 145 (2023) 13–23

Contents lists available at ScienceDirect

Computers and Mathematics with Applications

journal homepage: www.elsevier.com/locate/camwa

A new Poisson-type equation applicable to the three-dimensional non-hydrostatic model in the framework of the discontinuous Galerkin method

Guoquan Ran [a,b], Qinghe Zhang [a,*], Gaochuang Shi [a], Xia Li [b]

[a] State Key Laboratory of Hydraulic Engineering Simulation and Safety, Tianjin University, Tianjin 300072, China
[b] School of River and Ocean Engineering, Chongqing Jiaotong University, Chongqing 400074, China

ARTICLE INFO

Keywords:
Terrain-following σ-coordinate
Three-dimensional non-hydrostatic model
Poisson-type equation

ABSTRACT

In this study, a new Poisson-type equation for non-hydrostatic pressure in terrain-following σ-coordinates is proposed. The resulting equation consists of a standard elliptic operator and other first-order operators for non-hydrostatic pressure. Compared with the original Poisson-type equation, the treatment of the boundary condition at the lateral boundary can be simplified. Numerical tests indicate that the reformulated Poisson-type equation shows better convergence properties than the original equation when the quadrature-free nodal discontinuous Galerkin method is adopted for numerical discretization. Additionally, for the standing wave case, the numerical error of the three-dimensional non-hydrostatic model with the reformulated Poisson equation is smaller than that with the original equation, the numerical results of the solitary wave case indicate that the dissipation of the three-dimensional non-hydrostatic model is small, and transformation of wave over a circular shoal indicates that the developed model can properly simulate combined wave refraction and diffraction.

1. Introduction

The incompressible Navier-Stokes equation-based three-dimensional non-hydrostatic model has been widely used for the simulation of surface water waves [1–8] over the last two decades. This model is attractive due to the following properties. On the one hand, the elevation of the free surface is supposed to be a single-valued function of horizontal functions and can be captured by the free surface equation or the kinematic condition at the surface, so this model is not computationally expensive compared with the volume of fluid (VOF)-based [9], level set-based [10] or marker and cell (MAC)-based [11] numerical models and can be used for large-scale simulations. On the other hand, the model can reflect the nonlinearity and dispersion properties of water waves at variable water depths well since an arbitrary number of layers can be used in the vertical direction.

For the solution of the non-hydrostatic model, to avoid a system of equations of indefinite saddle point type arising from the coupling of velocity and pressure [12], this model is mainly solved numerically with the fraction-step method, and the whole process consists of a hydrostatic step and non-hydrostatic step. In the hydrostatic step, the nonlinear convection-diffusion equations for velocity are advanced in time to obtain the divergent velocity field, while in the non-hydrostatic step, a Poisson-type equation is numerically solved to obtain the non-hydrostatic pressure, which is further used for the correction of the divergent velocity field so that the final velocity field is divergence free. At present, for the widely used terrain-following σ-coordinate non-hydrostatic models, the following Poisson-type equation generally needs to be solved in the non-hydrostatic step [5,13,14]:

$$\frac{\partial^2 q}{\partial x^2}+\frac{\partial^2 q}{\partial y^2}+\left(\left(\frac{\partial \sigma}{\partial x^*}\right)^2+\left(\frac{\partial \sigma}{\partial y^*}\right)^2+\left(\frac{\partial \sigma}{\partial z^*}\right)^2\right)\frac{\partial^2 q}{\partial \sigma^2}$$
$$+2\left(\frac{\partial \sigma}{\partial x^*}\frac{\partial}{\partial x}\left(\frac{\partial q}{\partial \sigma}\right)+\frac{\partial \sigma}{\partial y^*}\frac{\partial}{\partial y}\left(\frac{\partial q}{\partial \sigma}\right)\right)+\left(\frac{\partial^2 \sigma}{\partial x \partial x^*}+\frac{\partial^2 \sigma}{\partial y \partial y^*}\right)\frac{\partial q}{\partial \sigma}$$
$$=\mathrm{RHS}, \tag{1}$$

where q is the non-hydrostatic pressure, x^*, y^* and z^* are the Cartesian coordinates in the physical domain, x, y and σ are the Cartesian coordinates in the computational domain, and RHS is the right-hand side of the Poisson-type equation. Eq. (1) has been numerically solved based on the finite difference method [14], finite volume method [13] and continuous Galerkin method [5].

* Corresponding author.
E-mail address: qhzhang@tju.edu.cn (Q. Zhang).

https://doi.org/10.1016/j.camwa.2023.06.003
Received 13 March 2022; Received in revised form 3 June 2023; Accepted 5 June 2023
Available online 19 June 2023

In recent years, the discontinuous Galerkin (DG) method has been used for the numerical implementation of incompressible Navier-Stokes equations [15,16] due to its local conservation, compactness, high order of accuracy and good application to unstructured meshes. When DG is used for the numerical implementation of the three-dimensional non-hydrostatic model and the boundary condition for the non-hydrostatic pressure is imposed weakly in the non-hydrostatic step, we need to explicitly impose the boundary condition for each term in Eq. (1), which is cumbersome and may introduce extensive numerical error. To simplify the numerical implementation of the boundary condition for the non-hydrostatic pressure, it is worthwhile to find a new way of handling the terms evolved in the derivation of the Poisson-type equation, with the goal of ultimately deriving a new form of Poisson-type equation. Therefore, the objective of the present paper is to derive a new type of Poisson-type equation consisting of a standard elliptic operator and other first-order operators for non-hydrostatic pressure. In the framework of the quadrature-free DG method, we numerically indicate that the newly derived Poisson-type equation shows better convergence properties and smaller numerical error and dissipation than the original equation.

This paper is organised as follows. In Section 2, the governing equations for the three-dimensional non-hydrostatic model in the terrain-following σ coordinate are derived based on the incompressible Navier–Stokes equations, and the accompanying boundary condition for non-hydrostatic pressure is given. In Section 3, the newly derived Poisson-type equation for non-hydrostatic pressure is derived first, followed by a comparison between the newly derived equation and the traditional equation. Numerical implementation of the reformulated Poisson equation is given in Section 4, and a comparison of the two different Poisson-type equations is conducted in Section 5. Finally, conclusions are drawn in Section 6.

2. Governing equations of the non-hydrostatic model

2.1. Governing equations

The incompressible Navier–Stokes equations in the physical domain $(x_1^* = x^*,\ x_2^* = y^*,\ x_3^* = z^*)$ are as follows:

$$\frac{\partial u_i}{\partial x_i^*} = 0, \tag{2}$$

$$\frac{\partial u_i}{\partial t^*} + u_j \frac{\partial u_i}{\partial x_j^*} = -\frac{1}{\rho}\frac{\partial p}{\partial x_i^*} + g_i + \frac{\partial \tau_{ij}}{\partial x_j^*}, \tag{3}$$

where t^* is the time, $(i,j) = 1,2,3$, u_i is the velocity component in direction x_i^*, p is the total pressure, ρ is the water density, $g_i = -g\delta_{i3}$ is the acceleration term due to gravity, and τ_{ij} is the turbulent stress, which is taken to be zero in the present paper. For the water wave we are concerned with, Eq. (2) and Eq. (3) are subject to the following kinetic boundary conditions at the surface and bottom boundary:

$$w_\eta = \frac{d\eta}{dt^*} = \frac{\partial \eta}{\partial t^*} + u_\eta \frac{\partial \eta}{\partial x^*} + v_\eta \frac{\partial \eta}{\partial y^*}, \tag{4}$$

$$w_b = \frac{db}{dt^*} = u_b \frac{\partial b}{\partial x^*} + v_b \frac{\partial b}{\partial y^*}, \tag{5}$$

where $\eta(x^*, y^*, t^*)$ and $b(x^*, y^*)$ are the water surface and bottom elevation, respectively, and (u_η, v_η, w_η) and (u_b, v_b, w_b) are the velocity components of the fluid parcels at the surface and bottom boundary.

To better represent the bottom topography and water surface, the σ transformation developed by Phillips [17] is adopted:

$$t = t^*, \qquad x = x^*, \qquad y = y^*, \qquad \sigma = \frac{z^* - \eta(x^*, y^*, t^*)}{D(x^*, y^*, t^*)}, \tag{6}$$

where $D(x^*, y^*, t^*) = \eta(x^*, y^*, t^*) - b(x^*, y^*)$ is the total water depth.

According to the principle of chain differentiation, partial derivatives of variable $f = f(x^*, y^*, z^*, t^*)$ in the physical domain can be written in the following form in the computational domain:

$$\begin{aligned}
\frac{\partial f}{\partial t^*} &= \frac{\partial f}{\partial t} + \frac{\partial f}{\partial \sigma}\frac{\partial \sigma}{\partial t^*},\\
\frac{\partial f}{\partial x^*} &= \frac{\partial f}{\partial x} + \frac{\partial f}{\partial \sigma}\frac{\partial \sigma}{\partial x^*},\\
\frac{\partial f}{\partial y^*} &= \frac{\partial f}{\partial y} + \frac{\partial f}{\partial \sigma}\frac{\partial \sigma}{\partial y^*},\\
\frac{\partial f}{\partial z^*} &= \frac{\partial f}{\partial \sigma}\frac{\partial \sigma}{\partial z^*}.
\end{aligned} \tag{7}$$

Substituting Eq. (7) back into Eq. (2) and Eq. (3), we can arrive at the governing equations for the terrain-following σ-coordinate non-hydrostatic models as follows:

$$\frac{\partial D}{\partial t} + \frac{\partial Du}{\partial x} + \frac{\partial Dv}{\partial y} + \frac{\partial \omega}{\partial \sigma} = 0, \tag{8}$$

$$\frac{\partial \mathbf{U}}{\partial t} + \frac{\partial \mathbf{E}}{\partial x} + \frac{\partial \mathbf{G}}{\partial y} + \frac{\partial \mathbf{H}}{\partial \sigma} = \mathbf{S}_h + \mathbf{S}_p, \tag{9}$$

where $\mathbf{U} = (Du, Dv, Dw)^T$ are the conservative variables and $\mathbf{E}$, $\mathbf{G}$, and $\mathbf{H}$ are the flux terms in the x, y and σ directions, respectively, and are defined as

$$\mathbf{E} = \begin{pmatrix} Duu + \frac{1}{2}g\left(D^2 - b^2\right) \\ Duv \\ Duw \end{pmatrix}, \qquad \mathbf{G} = \begin{pmatrix} Duv \\ Dvv + \frac{1}{2}g\left(D^2 - b^2\right) \\ Dvw \end{pmatrix},$$

$$\mathbf{H} = \begin{pmatrix} u\omega \\ v\omega \\ w\omega \end{pmatrix}. \tag{10}$$

The source terms are given as

$$\mathbf{S}_h = \begin{pmatrix} -g\eta\frac{\partial b}{\partial x} \\ -g\eta\frac{\partial b}{\partial y} \\ 0 \end{pmatrix}, \qquad \mathbf{S}_p = \begin{pmatrix} -\frac{D}{\rho}\left(\frac{\partial q}{\partial x} + \frac{\partial q}{\partial \sigma}\frac{\partial \sigma}{\partial x^*}\right) \\ -\frac{D}{\rho}\left(\frac{\partial q}{\partial y} + \frac{\partial q}{\partial \sigma}\frac{\partial \sigma}{\partial y^*}\right) \\ -\frac{1}{\rho}\frac{\partial q}{\partial \sigma} \end{pmatrix}. \tag{11}$$

It is noted that the total pressure p is divided into two parts: the non-hydrostatic pressure q and the hydrostatic pressure $\rho g(\eta - z^*)$. ω is the vertical velocity defined in the σ coordinate and is given as

$$\omega = w - \left(\sigma\frac{\partial D}{\partial t} + \frac{\partial \eta}{\partial t}\right) - u\left(\sigma\frac{\partial D}{\partial x} + \frac{\partial \eta}{\partial x}\right) - v\left(\sigma\frac{\partial D}{\partial y} + \frac{\partial \eta}{\partial y}\right). \tag{12}$$

Integrating Eq. (2) from the bottom to the surface and applying the kinematic boundary condition (4)–(5), we obtain the governing equation over the whole water depth as

$$\frac{\partial D}{\partial t} + \frac{\partial D\bar{U}}{\partial x} + \frac{\partial D\bar{V}}{\partial y} = 0, \tag{13}$$

with $\bar{U} = \int_{-1}^{0} u d\sigma$ and $\bar{V} = \int_{-1}^{0} v d\sigma$.

2.2. Boundary condition

For non-hydrostatic pressure q, a homogeneous Dirichlet boundary condition is imposed at the water surface in the physical domain, i.e.,

$$q(x^*, y^*, \eta) = 0. \tag{14}$$

At other boundaries, the Neumann boundary condition for non-hydrostatic pressure is imposed. For the lateral boundary, a homogeneous Neumann boundary condition is imposed, i.e.,

$$\nabla^* q \cdot \boldsymbol{n}^* = 0, \tag{15}$$

where $\nabla^* = \left(\frac{\partial}{\partial x^*}, \frac{\partial}{\partial y^*}, \frac{\partial}{\partial z^*}\right)$ and $\boldsymbol{n}^* = \left(n_x^*, n_y^*, n_z^*\right)$ is the unit outward normal of the lateral boundary. At the bottom boundary, the boundary condition for non-hydrostatic pressure is derived directly according to Eq. (3), and the partial derivative of the non-hydrostatic pressure in each direction is given as

$$\frac{\partial q}{\partial x_i^*} = -\rho\left(\frac{\partial u_i}{\partial t^*} + u_j\frac{\partial u_i}{\partial x_j^*} - g_i + g\frac{\partial D}{\partial x_i^*}\right). \tag{16}$$

After the σ transformation, the homogeneous Dirichlet boundary condition remains the same:

$$q(x, y, 0) = 0. \tag{17}$$

The boundary condition for the lateral boundary must be transformed as well. According to Eq. (15) and Eq. (7), we have

$$\nabla_\sigma q \cdot \boldsymbol{n} = 0, \tag{18}$$

where $\nabla_\sigma = \left(\frac{\partial}{\partial x} + \frac{\partial}{\partial \sigma}\frac{\partial \sigma}{\partial x^*}, \frac{\partial}{\partial y} + \frac{\partial}{\partial \sigma}\frac{\partial \sigma}{\partial y^*}, \frac{\partial}{\partial \sigma}\frac{\partial \sigma}{\partial z^*}\right)$ and $\boldsymbol{n} = (n_x, n_y, n_\sigma)$ is the outward unit normal vector for the lateral boundary in the computational domain. Likewise, the partial derivative of the non-hydrostatic pressure on the bottom boundary in each direction can be derived from Eq. (7) and Eq. (16), and the details are omitted here.

3. Derivation of the new Poisson-type equation

In this part, we first give the time step method used in our model, followed by the derivation of the new Poisson-type equation. Finally, a comparison between the newly derived Poisson-type equation and the original equation is given.

3.1. Time stepping

The model is advanced in time using the two-stage second-order strong stability preserving Runge–Kutta scheme. The first stage of the scheme for Eq. (9) and Eq. (13) is as follows:

$$\frac{\mathbf{U}^* - \mathbf{U}^n}{\Delta t} = -\frac{\partial \mathbf{E}^n}{\partial x} - \frac{\partial \mathbf{G}^n}{\partial y} - \frac{\partial \mathbf{H}^n}{\partial \sigma} + \mathbf{S}_h^n, \tag{19}$$

$$\frac{D^{(1)} - D^n}{\Delta t} = -\frac{\partial (D\bar{U})^n}{\partial x} - \frac{\partial (D\bar{V})^n}{\partial y}, \tag{20}$$

$$\frac{\mathbf{U}^{(1)} - \mathbf{U}^*}{\Delta t} = \mathbf{S}_p^{(1)}(D^{(1)}, q^{(1)}). \tag{21}$$

The depth-averaged momenta $(D\bar{U})^n$ and $(D\bar{V})^n$ in Eq. (20) are obtained through the integration of $(Du)^n$ and $(Dv)^n$ over the total water depth. The temporary momentum $\mathbf{U}^*$ in Eq. (19) are not divergence free and need to be corrected through Eq. (21).

For the second stage of the scheme, the momentum and the water depth are further updated as

$$\frac{\mathbf{U}^* - \mathbf{U}^{(1)}}{\Delta t} = -\frac{\partial \mathbf{E}^{(1)}}{\partial x} - \frac{\partial \mathbf{G}^{(1)}}{\partial y} - \frac{\partial \mathbf{H}^{(1)}}{\partial \sigma} + \mathbf{S}_h^{(1)}, \tag{22}$$

$$\frac{D^{(2)} - D^{(1)}}{\Delta t} = -\frac{\partial (D\bar{U})^{(1)}}{\partial x} - \frac{\partial (D\bar{V})^{(1)}}{\partial y}, \tag{23}$$

$$\frac{\mathbf{U}^{(2)} - \mathbf{U}^*}{\Delta t} = \mathbf{S}_p^{(2)}(D^{(2)}, q^{(2)}). \tag{24}$$

The depth-averaged momenta $(D\bar{U})^{(1)}$ and $(D\bar{V})^{(1)}$ in Eq. (23) are also obtained through the integration of $(Du)^{(1)}$ and $(Dv)^{(1)}$ over the total water depth. Likewise, the temporary momentum $\mathbf{U}^*$ in Eq. (22) are not divergence free and need to be corrected through Eq. (24). With the results at the second stage at hand, we can obtain the variables at level $n+1$ as follows:

$$\mathbf{U}^{n+1} = \frac{1}{2}\mathbf{U}^n + \frac{1}{2}\mathbf{U}^{(2)}, \tag{25}$$

$$D^{n+1} = \frac{1}{2}D^n + \frac{1}{2}D^{(2)}. \tag{26}$$

In both stages, the temporary momentum $\mathbf{U}^*$ needs to be corrected. With the non-hydrostatic pressure q introduced, the system is no longer closed and needs to be solved together with the continuity equation. Combining Eq. (2) with Eq. (7), we obtain the continuity equation in the terrain-following σ-coordinate as

$$\frac{\partial u}{\partial x} + \frac{\partial u}{\partial \sigma}\frac{\partial \sigma}{\partial x^*} + \frac{\partial v}{\partial y} + \frac{\partial v}{\partial \sigma}\frac{\partial \sigma}{\partial y^*} + \frac{\partial w}{\partial \sigma}\frac{\partial \sigma}{\partial z^*} = 0. \tag{27}$$

For the convenience of description, derivation of the new form of Poisson equation is conducted based on the first stage of the scheme and Eq. (27). The same derivation also applies to the second stage of the scheme since corrections for both stages are the same.

3.2. Derivation of the new Poisson-type equation

Approximating the temporary water depth D^* within the temporary momentum $\mathbf{U}^*$ by $D^{(1)}$ and dividing it on both sides of Eq. (21), we have

$$\begin{aligned} u &= u^* - \frac{\Delta t}{\rho}\left(\frac{\partial q}{\partial x} + \frac{\partial q}{\partial \sigma}\frac{\partial \sigma}{\partial x^*}\right), \\ v &= v^* - \frac{\Delta t}{\rho}\left(\frac{\partial q}{\partial y} + \frac{\partial q}{\partial \sigma}\frac{\partial \sigma}{\partial y^*}\right), \\ w &= w^* - \frac{\Delta t}{\rho D}\left(\frac{\partial q}{\partial \sigma}\right). \end{aligned} \tag{28}$$

For the convenience of derivation, the superscripts for velocity components, i.e. u, v, and w, the water depth D, and non-hydrostatic pressure q are ignored in Eq. (28).

Substitution of Eq. (28) into Eq. (27) yields

$$\begin{aligned} &\frac{\partial}{\partial x}\left[u^* - \frac{\Delta t}{\rho}\left(\frac{\partial q}{\partial x} + \frac{\partial q}{\partial \sigma}\frac{\partial \sigma}{\partial x^*}\right)\right] + \frac{\partial}{\partial \sigma}\left[u^* - \frac{\Delta t}{\rho}\left(\frac{\partial q}{\partial x} + \frac{\partial q}{\partial \sigma}\frac{\partial \sigma}{\partial x^*}\right)\right]\frac{\partial \sigma}{\partial x^*} \\ &\quad + \frac{\partial}{\partial y}\left[v^* - \frac{\Delta t}{\rho}\left(\frac{\partial q}{\partial y} + \frac{\partial q}{\partial \sigma}\frac{\partial \sigma}{\partial y^*}\right)\right] \\ &\quad + \frac{\partial}{\partial \sigma}\left[v^* - \frac{\Delta t}{\rho}\left(\frac{\partial q}{\partial y} + \frac{\partial q}{\partial \sigma}\frac{\partial \sigma}{\partial y^*}\right)\right]\frac{\partial \sigma}{\partial y^*} + \frac{\partial}{\partial \sigma}\left[w^* - \frac{\Delta t}{\rho D}\left(\frac{\partial q}{\partial \sigma}\right)\right]\frac{\partial \sigma}{\partial z^*} \\ &= 0. \end{aligned} \tag{29}$$

Moving the known terms to the right-hand side, we transform Eq. (29) to

$$\begin{aligned} &\frac{\partial}{\partial x}\left[\frac{\partial q}{\partial x} + \frac{\partial q}{\partial \sigma}\frac{\partial \sigma}{\partial x^*}\right] + \frac{\partial}{\partial \sigma}\left[\frac{\partial q}{\partial x} + \frac{\partial q}{\partial \sigma}\frac{\partial \sigma}{\partial x^*}\right]\frac{\partial \sigma}{\partial x^*} + \frac{\partial}{\partial y}\left[\frac{\partial q}{\partial y} + \frac{\partial q}{\partial \sigma}\frac{\partial \sigma}{\partial y^*}\right] \\ &\quad + \frac{\partial}{\partial \sigma}\left[\frac{\partial q}{\partial y} + \frac{\partial q}{\partial \sigma}\frac{\partial \sigma}{\partial y^*}\right]\frac{\partial \sigma}{\partial y^*} + \left(\frac{\partial \sigma}{\partial z^*}\right)^2\frac{\partial^2 q}{\partial \sigma^2} \\ &= \frac{\rho}{\Delta t}\left(\frac{\partial u^*}{\partial x} + \frac{\partial u^*}{\partial \sigma}\frac{\partial \sigma}{\partial x^*} + \frac{\partial v^*}{\partial y} + \frac{\partial v^*}{\partial \sigma}\frac{\partial \sigma}{\partial y^*} + \frac{1}{D}\frac{\partial w^*}{\partial \sigma}\right). \end{aligned} \tag{30}$$

The second, fourth and fifth terms in Eq. (30) can be expanded as follows:

$$\begin{aligned} &\frac{\partial}{\partial \sigma}\left[\frac{\partial q}{\partial x} + \frac{\partial q}{\partial \sigma}\frac{\partial \sigma}{\partial x^*}\right]\frac{\partial \sigma}{\partial x^*} \\ &= \frac{\partial}{\partial \sigma}\left[\frac{\partial \sigma}{\partial x^*}\frac{\partial q}{\partial x}\right] - \frac{\partial q}{\partial x}\frac{\partial}{\partial \sigma}\left(\frac{\partial \sigma}{\partial x^*}\right) + \left(\frac{\partial \sigma}{\partial x^*}\right)^2\frac{\partial^2 q}{\partial \sigma^2} + \frac{\partial q}{\partial \sigma}\frac{\partial \sigma}{\partial x^*}\frac{\partial}{\partial \sigma}\left(\frac{\partial \sigma}{\partial x^*}\right) \\ &= \frac{\partial}{\partial \sigma}\left[\frac{\partial \sigma}{\partial x^*}\frac{\partial q}{\partial x}\right] - \frac{\partial q}{\partial x}\frac{\partial}{\partial \sigma}\left(\frac{\partial \sigma}{\partial x^*}\right) + \frac{\partial}{\partial \sigma}\left[\left(\frac{\partial \sigma}{\partial x^*}\right)^2\frac{\partial q}{\partial \sigma}\right] - \frac{\partial q}{\partial \sigma}\frac{\partial}{\partial \sigma}\left[\left(\frac{\partial \sigma}{\partial x^*}\right)^2\right] \\ &\quad + \frac{\partial q}{\partial \sigma}\frac{\partial \sigma}{\partial x^*}\frac{\partial}{\partial \sigma}\left(\frac{\partial \sigma}{\partial x^*}\right) \\ &= \frac{\partial}{\partial \sigma}\left[\frac{\partial \sigma}{\partial x^*}\frac{\partial q}{\partial x}\right] - \frac{\partial q}{\partial x}\frac{\partial}{\partial \sigma}\left(\frac{\partial \sigma}{\partial x^*}\right) + \frac{\partial}{\partial \sigma}\left[\left(\frac{\partial \sigma}{\partial x^*}\right)^2\frac{\partial q}{\partial \sigma}\right] \\ &\quad - \frac{\partial q}{\partial \sigma}\frac{\partial \sigma}{\partial x^*}\frac{\partial}{\partial \sigma}\left(\frac{\partial \sigma}{\partial x^*}\right) \end{aligned} \tag{31}$$

$$\begin{aligned} &\frac{\partial}{\partial \sigma}\left[\frac{\partial q}{\partial y} + \frac{\partial q}{\partial \sigma}\frac{\partial \sigma}{\partial y^*}\right]\frac{\partial \sigma}{\partial y^*} \\ &= \frac{\partial}{\partial \sigma}\left[\frac{\partial \sigma}{\partial y^*}\frac{\partial q}{\partial y}\right] - \frac{\partial q}{\partial y}\frac{\partial}{\partial \sigma}\left(\frac{\partial \sigma}{\partial y^*}\right) + \left(\frac{\partial \sigma}{\partial y^*}\right)^2\frac{\partial^2 q}{\partial \sigma^2} + \frac{\partial q}{\partial \sigma}\frac{\partial \sigma}{\partial y^*}\frac{\partial}{\partial \sigma}\left(\frac{\partial \sigma}{\partial y^*}\right) \\ &= \frac{\partial}{\partial \sigma}\left[\frac{\partial \sigma}{\partial y^*}\frac{\partial q}{\partial y}\right] - \frac{\partial q}{\partial y}\frac{\partial}{\partial \sigma}\left(\frac{\partial \sigma}{\partial y^*}\right) + \frac{\partial}{\partial \sigma}\left[\left(\frac{\partial \sigma}{\partial y^*}\right)^2\frac{\partial q}{\partial \sigma}\right] \\ &\quad - \frac{\partial q}{\partial \sigma}\frac{\partial}{\partial \sigma}\left[\left(\frac{\partial \sigma}{\partial y^*}\right)^2\right] + \frac{\partial q}{\partial \sigma}\frac{\partial \sigma}{\partial y^*}\frac{\partial}{\partial \sigma}\left(\frac{\partial \sigma}{\partial y^*}\right) \\ &= \frac{\partial}{\partial \sigma}\left[\frac{\partial \sigma}{\partial y^*}\frac{\partial q}{\partial y}\right] - \frac{\partial q}{\partial y}\frac{\partial}{\partial \sigma}\left(\frac{\partial \sigma}{\partial y^*}\right) + \frac{\partial}{\partial \sigma}\left[\left(\frac{\partial \sigma}{\partial y^*}\right)^2\frac{\partial q}{\partial \sigma}\right] \end{aligned}$$

$$-\frac{\partial q}{\partial \sigma}\frac{\partial \sigma}{\partial y^*}\frac{\partial}{\partial \sigma}\left(\frac{\partial \sigma}{\partial y^*}\right) \tag{32}$$

$$\left(\frac{\partial \sigma}{\partial z^*}\right)^2\frac{\partial^2 q}{\partial \sigma^2}=\frac{\partial}{\partial \sigma}\left(\left(\frac{\partial \sigma}{\partial z^*}\right)^2\frac{\partial q}{\partial \sigma}\right). \tag{33}$$

Substituting Eq. (31) to Eq. (33) into Eq. (30), the final Poisson-type equation is given as

$$\nabla\cdot\mathbf{K}\nabla q-\nabla q\cdot\boldsymbol{u}_\sigma=\frac{\rho}{\Delta t}\left(\frac{\partial u^*}{\partial x}+\frac{\partial u^*}{\partial \sigma}\frac{\partial \sigma}{\partial x^*}+\frac{\partial v^*}{\partial y}+\frac{\partial v^*}{\partial \sigma}\frac{\partial \sigma}{\partial y^*}+\frac{1}{D}\frac{\partial w^*}{\partial \sigma}\right), \tag{34}$$

where $\nabla=\left(\frac{\partial}{\partial x},\frac{\partial}{\partial y},\frac{\partial}{\partial \sigma}\right)$ is the three-dimensional divergence operator in the computational domain, $\mathbf{K}$ is a symmetric positive-definite diffusion matrix with components varying in space and time and is defined as

$$\mathbf{K}=\begin{bmatrix}1 & 0 & \partial\sigma/\partial x^*\\ 0 & 1 & \partial\sigma/\partial y^*\\ \partial\sigma/\partial x^* & \partial\sigma/\partial y^* & (\partial\sigma/\partial x^*)^2+(\partial\sigma/\partial y^*)^2+(\partial\sigma/\partial z^*)^2\end{bmatrix}, \tag{35}$$

and $\boldsymbol{u}_\sigma$ is a vector composed of derivatives or partial derivatives about σ, and is defined as

$$\boldsymbol{u}_\sigma=\left(\frac{\partial}{\partial \sigma}\left(\frac{\partial \sigma}{\partial x^*}\right),\frac{\partial}{\partial \sigma}\left(\frac{\partial \sigma}{\partial y^*}\right),\frac{\partial \sigma}{\partial x^*}\frac{\partial}{\partial \sigma}\left(\frac{\partial \sigma}{\partial x^*}\right)+\frac{\partial \sigma}{\partial y^*}\frac{\partial}{\partial \sigma}\left(\frac{\partial \sigma}{\partial y^*}\right)\right). \tag{36}$$

According to Eq. (6), these terms can be explicitly given as

$$\begin{aligned}\frac{\partial \sigma}{\partial x^*}&=-\frac{1}{D}\left(\frac{\partial b}{\partial x^*}+\frac{\partial D}{\partial x^*}\right)-\frac{\sigma}{D}\frac{\partial D}{\partial x^*},\\ \frac{\partial \sigma}{\partial y^*}&=-\frac{1}{D}\left(\frac{\partial b}{\partial y^*}+\frac{\partial D}{\partial y^*}\right)-\frac{\sigma}{D}\frac{\partial D}{\partial y^*},\end{aligned} \tag{37}$$

$$\frac{\partial}{\partial \sigma}\left(\frac{\partial \sigma}{\partial x^*}\right)=-\frac{1}{D}\frac{\partial D}{\partial x^*},\qquad \frac{\partial}{\partial \sigma}\left(\frac{\partial \sigma}{\partial y^*}\right)=-\frac{1}{D}\frac{\partial D}{\partial y^*}. \tag{38}$$

3.3. Comparison of the two types of Poisson type equations

The difference between Eq. (1) and Eq. (34) lies in the treatment of the Neumann boundary condition for non-hydrostatic pressure. For the second-order operator in Eq. (34), the Neumann boundary condition is given as

$$\begin{aligned}\mathbf{K}\nabla q\cdot\boldsymbol{n}=&\left(\frac{\partial q}{\partial x}+\frac{\partial q}{\partial \sigma}\frac{\partial \sigma}{\partial x^*}\right)n_x+\left(\frac{\partial q}{\partial y}+\frac{\partial q}{\partial \sigma}\frac{\partial \sigma}{\partial y^*}\right)n_y\\ &+\left(\frac{\partial \sigma}{\partial x^*}\frac{\partial q}{\partial x}+\frac{\partial \sigma}{\partial y^*}\frac{\partial q}{\partial y}+\left(\left(\frac{\partial \sigma}{\partial x^*}\right)^2+\left(\frac{\partial \sigma}{\partial y^*}\right)^2+\left(\frac{\partial \sigma}{\partial z^*}\right)^2\right)\frac{\partial q}{\partial \sigma}\right)\\ &\times n_\sigma.\end{aligned} \tag{39}$$

For the lateral boundary with $n_x=n_x^*$, $n_y=n_y^*$, $n_\sigma=0$ (see the description in Section 4.1), Eq. (39) is equivalent to Eq. (18), so the Neumann boundary condition can maintain the original form of the Neumann boundary condition with σ transformation considered and has no effect on the final stiff matrix or the right-hand side (details about this can be found from the numerical implementation in Section 4.2). At the bottom boundary, the components of the outward unit normal vector of the computational domain are $n_x=0$, $n_y=0$, and $n_\sigma=-1$, and only the third term on the right-hand side of Eq. (39) is nonzero. Considering that σ equals -1 at the bottom boundary, the partial derivatives of σ with respect to x^* and y^* can be further simplified as

$$\frac{\partial \sigma}{\partial x^*}=-\frac{1}{D}\frac{\partial b}{\partial x^*},\qquad \frac{\partial \sigma}{\partial y^*}=-\frac{1}{D}\frac{\partial b}{\partial y^*}. \tag{40}$$

No partial derivative terms referring to water depth are included in Eq. (40), and possible numerical error due to this part can be avoided.

In contrast to the newly derived Poisson-type equation, the original Poisson-type equation, Eq. (1), is much more complex in regard to imposing the Neumann boundary condition. At the lateral boundary, the term $\partial q/\partial x n_x+\partial q/\partial y n_y$ needs to be given explicitly for the first two terms on the left-hand side of Eq. (1). This term can be calculated in the following two ways. In the first method, it is directly given according to Eq. (7) and Eq. (16), i.e., incompressible Navier–Stokes equations in the terrain-following σ-coordinate, while in the second method, it is set as

$$-\frac{\partial q}{\partial \sigma}\frac{\partial \sigma}{\partial x^*}n_x-\frac{\partial q}{\partial \sigma}\frac{\partial \sigma}{\partial y^*}n_y, \tag{41}$$

according to Eq. (18).

In both methods, the calculation of $\partial\sigma/\partial x^*$ and $\partial\sigma/\partial y^*$ cannot be simplified since σ varies between -1 and 0. In addition, in the numerical discretization of mixed partial derivatives referring to non-hydrostatic pressure in Eq. (1), $\partial q/\partial\sigma n_x$ and $\partial q/\partial\sigma n_y$ need to be appointed at the lateral boundary, and the $\partial q/\partial\sigma$ in these two terms can be calculated only according to the incompressible Navier–Stokes equations in the terrain-following σ-coordinate. At the bottom boundary, the term $\partial q/\partial\sigma n_\sigma$ needs to be given, which also needs to be calculated based on the incompressible Navier–Stokes equations in the terrain-following σ-coordinate. Generally, all of these terms are nonzero and contribute to the right-hand side of the global linear system.

4. Numerical implementation

In this part, we first describe the domain partition and the discontinuous polynomial space related to it. Then, the numerical implementation of Eq. (34) based on the quadrature-free DG method is given.

4.1. Domain partition and polynomial space

For an arbitrary three-dimensional domain Ω_{3d}, its horizontal projection is denoted as Ω_{2d} and is partitioned by $N_{ele,2d}$ non-overlapping triangular or quadrilateral elements; i.e., $\Omega_{2d}=\left\{\Omega_{2d}^e : e\in\left[1,N_{ele,2d}\right]\right\}$. In the vertical direction, Ω_{2d} is extruded by N_L layers to obtain the three-dimensional computational domain $\Omega_{3d}=\left\{\Omega^e : e\in[1,N_{ele}]\right\}$, where $N_{ele}=N_{ele,2d}\times N_L$ is the number of elements and the final three-dimensional computational domain consists of triangular prisms or quadrangular prisms. In Fig. 1, a schematic view of two columns of nodal elements is given with a horizontal approximation order $N_h=1$, vertical approximation order $N_v=2$, and vertical layers $N_L=2$. And the interpolation nodes set defined over the elements is the tensor product of the one-dimensional (1D) Legendre-Gauss-Lobatto (LGL) quadrature points and two-dimensional (2D) nodes set [18]. At the topmost ($\sigma=0$) and bottommost ($\sigma=-1$) boundaries of the computational domain, the horizontal components of the unit outward normal are zero; i.e., $n_x=n_y=0$. Additionally, the horizontal components of the unit outward normal at the lateral boundary of the computational domain are equal to those of the physical domain. $n_x=n_x^*$, and $n_y=n_y^*$ since only the vertical coordinate is stretched or compressed in the σ transformation.

In addition, we introduce the following finite dimensional space of polynomials:

$$V_h=\left\{s\in L^2(\Omega):\forall\Omega^e\in\Omega_{3d},s\in\mathcal{P}_{(N_h,N_v)}(\Omega^e)\right\}, \tag{42}$$

where $L^2(\Omega)$ is the space of the square-integrable functions and $\mathcal{P}_{(N_h,N_v)}(\Omega^e)$ is the complete space of polynomials defined over Ω^e, which is of order at most N_h in the horizontal direction and at most N_v in the vertical direction. Let ϵ_I be the union of the unique interior edge of the computational domain, and let ϵ_B be the union of the unique boundary edge. For any two adjacent elements Ω^{e-} and Ω^{e+}, let $f_{e^-/e^+}=\partial\Omega^{e-}\cap\partial\Omega^{e+}$ be the interface between them, and let $\boldsymbol{n}^-=(n_x^-,n_y^-,n_\sigma^-)$ and $\boldsymbol{n}^+=(n_x^+,n_y^+,n_\sigma^+)$ be the outward unit normal vector on the interface. For scalar field $c\in V_h$ and vector field $\mathbf{a}\in V_h^3$, let $c^\pm$ and $\mathbf{a}^\pm$ be the traces of c and $\mathbf{a}$ on f_{e^-/e^+} from the interior of Ω^{e-} and Ω^{e+}. We further define the average operator $\{\cdot\}$ and jump operator $[\cdot]$ as follows:

$$\begin{aligned}\{c\}&=\frac{c^++c^-}{2},\qquad [c]=c^+\boldsymbol{n}^++c^-\boldsymbol{n}^-,\\ \{\mathbf{a}\}&=\frac{\mathbf{a}^++\mathbf{a}^-}{2},\qquad [\mathbf{a}]=\mathbf{a}^+\cdot\boldsymbol{n}^++\mathbf{a}^-\cdot\boldsymbol{n}^-.\end{aligned} \tag{43}$$

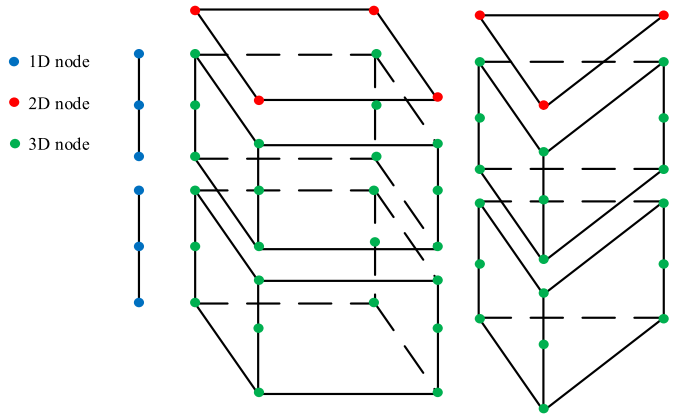

Fig. 1. Schematic view of two columns of three-dimensional computational elements, quadrangular prisms (left) and triangular prisms (right). For illustration purposes, the discontinuities between the adjacent computational elements have been exaggerated, and no gap exists in reality.

On the union of the boundary edges, ϵ_B, these terms are defined as

$$\{c\} = c, \qquad [c] = c\boldsymbol{n},$$
$$\{\mathbf{a}\} = \mathbf{a}, \qquad [\mathbf{a}] = \mathbf{a}\cdot\boldsymbol{n}, \tag{44}$$

where c and $\mathbf{a}$ are the unique values and $\boldsymbol{n}$ is the unit outward normal of ϵ_B.

4.2. Numerical implementation

For the numerical implementation of Eq. (34), we start from the following elliptic problem:

$$\begin{aligned}
&\nabla\cdot\mathbf{K}\nabla q(\boldsymbol{x}) = f(\boldsymbol{x}) \quad \boldsymbol{x}\in\Omega_{3d},\\
&q(\boldsymbol{x}) = q_D(\boldsymbol{x}) \quad \boldsymbol{x}\in\varepsilon_B^D,\\
&(\mathbf{K}\nabla q(\boldsymbol{x}))\cdot\boldsymbol{n} = q_N(\boldsymbol{x}) \quad \boldsymbol{x}\in\varepsilon_B^N,
\end{aligned} \tag{45}$$

where $\varepsilon_B^D \neq \phi$ and ε_B^N are the Dirichlet boundary and Neumann boundary with respect to the non-hydrostatic pressure respectively, and $\varepsilon_B^D \cup \varepsilon_B^N = \varepsilon_B$. Eq. (45) is first recast into the following first-order system of equations:

$$\begin{aligned}
&\nabla\cdot\mathbf{Q} = f(\boldsymbol{x}) \quad \boldsymbol{x}\in\Omega_{3d},\\
&\mathbf{Q} = \mathbf{K}\nabla q(\boldsymbol{x}) \quad \boldsymbol{x}\in\Omega_{3d},\\
&q(\boldsymbol{x}) = q_D(\boldsymbol{x}) \quad \boldsymbol{x}\in\varepsilon_B^D,\\
&\mathbf{Q}\cdot\boldsymbol{n} = q_N(\boldsymbol{x}) \quad \boldsymbol{x}\in\varepsilon_B^N.
\end{aligned} \tag{46}$$

We find $q_h \in V_h$ and $\mathbf{Q}_h \in V_h^3$ such that for all $\Omega^e \in \Omega_{3d}$, we have

$$\int_{\Omega^e}\mathbf{Q}_h\cdot\boldsymbol{\tau}d\boldsymbol{x} = -\int_{\Omega^e} q_h\nabla_h\cdot(\mathbf{K}\boldsymbol{\tau})\,d\boldsymbol{x} + \int_{\partial\Omega^e}\hat{q}_h\mathbf{K}\boldsymbol{\tau}\cdot\boldsymbol{n}d\boldsymbol{x}, \quad \forall\boldsymbol{\tau}\in V_h^3 \tag{47}$$

$$-\int_{\Omega^e}\mathbf{Q}_h\cdot\nabla_h v d\boldsymbol{x} = \int_{\Omega^e} f v d\boldsymbol{x} - \int_{\partial\Omega^e} v\hat{\mathbf{Q}}_h\cdot\boldsymbol{n}d\boldsymbol{x}, \quad \forall v\in V_h \tag{48}$$

Here, ∇_h is the broken gradient operator, $\hat{q}_h$ and $\hat{\mathbf{Q}}_h$ are the numerical fluxes, and are approximations of $q(\boldsymbol{x})$ and $\mathbf{Q} = \mathbf{K}\nabla q(\boldsymbol{x})$ at the elemental boundaries, respectively. On the interior face, the numerical fluxes are given as

$$\hat{\mathbf{Q}}_h = \{\mathbf{K}\nabla_h q_h\}_\omega - \tau[q_h], \quad \hat{q}_h = \{q_h\}, \tag{49}$$

where $\{\mathbf{K}\nabla_h q_h\}_\omega$ is the weighted average defined as

$$\{\mathbf{K}\nabla_h q_h\}_\omega = \omega^-(\mathbf{K}\nabla_h q_h)^- + \omega^+(\mathbf{K}\nabla_h q_h)^+, \tag{50}$$

and the two nonnegative real numbers ω^- and ω^+ are the weights on the interior face as,

$$\omega^- = \frac{\kappa^+}{\kappa^- + \kappa^+}, \qquad \omega^+ = \frac{\kappa^-}{\kappa^- + \kappa^+}, \tag{51}$$

with $\kappa^\pm = (\boldsymbol{n}^\pm)^T\boldsymbol{K}\boldsymbol{n}^\pm$ the normal component of the diffusion matrix on both sides of the interior face f_{e^-/e^+}. Also, τ in Eq. (49) is the penalty parameter defined as,

$$\tau = \frac{\eta}{h_F}\frac{2\kappa^-\kappa^+}{\kappa^- + \kappa^+}, \tag{52}$$

where η is a user-dependent parameter and is set to be 1000 in this study, h_F is a local length scale associated with the mesh face [19].

On the boundary faces, the corresponding numerical fluxes are given as,

$$\hat{\mathbf{Q}}_h = \mathbf{K}\nabla_h q_h - \tau(q_h - q_D)\boldsymbol{n}, \qquad \hat{q}_h = q_D, \qquad \boldsymbol{x}\in\varepsilon_B^D \tag{53}$$

$$\hat{\mathbf{Q}}_h = q_N\boldsymbol{n}, \qquad \hat{q}_h = q_h, \qquad \boldsymbol{x}\in\varepsilon_B^N \tag{54}$$

with τ calculated according to Eq. (52) by setting $\kappa^+ = \kappa^- = \boldsymbol{n}^T\boldsymbol{K}\boldsymbol{n}$.

Summing Eqs. (47) and (48) over the computational domain, we have

$$\begin{aligned}
\int_{\Omega_{3d}}\mathbf{Q}_h\cdot\boldsymbol{\tau}d\boldsymbol{x} = &-\int_{\Omega_{3d}} q_h\nabla_h\cdot(\mathbf{K}\boldsymbol{\tau})\,d\boldsymbol{x} + \int_{\epsilon_I}\hat{q}_h[\mathbf{K}\boldsymbol{\tau}]\,d\boldsymbol{x}\\
&+\int_{\epsilon_B}\hat{q}_h\mathbf{K}\boldsymbol{\tau}\cdot\boldsymbol{n}d\boldsymbol{x} \quad \forall\boldsymbol{\tau}\in V_h^3,
\end{aligned} \tag{55}$$

$$-\int_{\Omega_{3d}}\mathbf{Q}_h\cdot\nabla_h v d\boldsymbol{x} = \int_{\Omega_{3d}} f v d\boldsymbol{x} - \int_{\epsilon_I}\hat{\mathbf{Q}}_h\cdot[v]\,d\boldsymbol{x} - \int_{\epsilon_B} v\hat{\mathbf{Q}}_h\cdot\boldsymbol{n}d\boldsymbol{x} \quad \forall v\in V_h. \tag{56}$$

Substituting the numerical fluxes, and after some manipulation, we can obtain the primal form about the non-hydrostatic pressure as

$$\begin{aligned}
&-\int_{\Omega_{3d}}\nabla_h v\cdot(\mathbf{K}\nabla_h q_h)\,d\boldsymbol{x} + \int_{\epsilon_I}[q_h]\cdot\{\mathbf{K}\nabla_h v\}_\omega\,d\boldsymbol{x}\\
&+\int_{\epsilon_I}(\{\mathbf{K}\nabla_h q_h\}_\omega - \tau[q_h])\cdot[v]\,d\boldsymbol{x}\\
&+\int_{\varepsilon_B^D} q_h\mathbf{K}\nabla_h v\cdot\boldsymbol{n}d\boldsymbol{x} + \int_{\varepsilon_B^D} v\mathbf{K}\nabla_h q_h\cdot\boldsymbol{n}d\boldsymbol{x} - \int_{\varepsilon_B^D}\tau u_h v d\boldsymbol{x} = \int_{\Omega_{3d}} f v d\boldsymbol{x}\\
&+\int_{\varepsilon_B^D} q_D\mathbf{K}\nabla_h v\cdot\boldsymbol{n}d\boldsymbol{x} + \int_{\varepsilon_B^D}\tau q_D v d\boldsymbol{x} - \int_{\varepsilon_B^N} v q_N d\boldsymbol{x}.
\end{aligned} \tag{57}$$

A thorough a *priori* error analysis yielding robust and optimal error estimates for the above primal form has been conducted by Ern et al. in [20].

Apart from the second-order operator for non-hydrostatic pressure, the first-order partial derivatives are included in Eq. (34). For the discretization of these terms, we introduce the following auxiliary variable:

$$\boldsymbol{\sigma} = \nabla q. \tag{58}$$

For Eq. (58), we find $(q_h, \boldsymbol{\sigma}_h) \in V_h \times V_h^3$ such that for all elements $\Omega^e \in \Omega_{3d}$ and $\boldsymbol{\tau}\in V_h^3$, we have

$$\int_{\Omega^e}\boldsymbol{\sigma}_h\cdot\boldsymbol{\tau}d\boldsymbol{x} = -\int_{\Omega^e} q_h\nabla_h\cdot\boldsymbol{\tau}d\boldsymbol{x} + \int_{\partial\Omega^e}\hat{q}_h\boldsymbol{\tau}\cdot\boldsymbol{n}d\boldsymbol{x}, \quad \forall\boldsymbol{\tau}\in V_h^3 \tag{59}$$

Here, $\hat{q}_h$ is the numerical approximation to q_h at the elemental boundaries and is given in Eqs. (49), (53) and (54). Summing Eq. (59) over the computational domain and applying the integration by part, we have

$$\int_{\Omega_{3d}}\boldsymbol{\sigma}_h\cdot\boldsymbol{\tau}d\boldsymbol{x} = \int_{\Omega_{3d}}\boldsymbol{\tau}\cdot\nabla_h q_h d\boldsymbol{x} - \int_{\epsilon_I}([q_h]\cdot\{\boldsymbol{\tau}\} - \{\hat{q}_h - q_h\}[\boldsymbol{\tau}])\,d\boldsymbol{x}$$

$$+\int_{\epsilon_B}\left(\hat{q}_h-q_h\right)\boldsymbol{\tau}\cdot\boldsymbol{n}d\boldsymbol{x},\quad \forall\boldsymbol{\tau}\in V_h^3 \tag{60}$$

Substituting the numerical flux into Eq. (57), we arrive at

$$\int_{\Omega_{3d}}\boldsymbol{\sigma}_h\cdot\boldsymbol{\tau}d\boldsymbol{x}=\int_{\Omega_{3d}}\boldsymbol{\tau}\cdot\nabla_h q_h d\boldsymbol{x}-\int_{\epsilon_I}\left[q_h\right]\cdot\{\boldsymbol{\tau}\}\,d\boldsymbol{x}+\int_{\epsilon_B^D}\left(q_D-q_h\right)\boldsymbol{\tau}\cdot\boldsymbol{n}d\boldsymbol{x},$$
$$\forall\boldsymbol{\tau}\in V_h^3 \tag{61}$$

Defining the lifting operators $\mathbf{r}:L^2\left(\epsilon_I\right)\to V_h^3$ and $\mathbf{r}_D:L^2\left(\epsilon_B^D\right)\to V_h^3$,

$$\int_{\Omega_{3d}}\mathbf{r}\left(\phi\right)\cdot\boldsymbol{\tau}d\boldsymbol{x}=-\int_{\epsilon_I}\phi\cdot\{\boldsymbol{\tau}\}\,d\boldsymbol{x}\quad\forall\boldsymbol{\tau}\in V_h^3,$$
$$\int_{\Omega_{3d}}\mathbf{r}_D\left(q\right)\cdot\boldsymbol{\tau}d\boldsymbol{x}=-\int_{\epsilon_B^D}q\boldsymbol{\tau}\cdot\boldsymbol{n}d\boldsymbol{x}\quad\forall\boldsymbol{\tau}\in V_h^3, \tag{62}$$

we have

$$\boldsymbol{\sigma}_h=\nabla_h q_h+\mathbf{r}\left(\left[q_h\right]\right)-\mathbf{r}_D\left(q_D-q_h\right). \tag{63}$$

It can be seen that $\boldsymbol{\sigma}_h$ is equal to $\nabla_h q_h$ plus additional perturbation terms forced by $\left[q_h\right]$ and q_D-q_h.

For the discretization of Eqs (57) and (63), the solution on each element is approximated by a finite series expansion as,

$$q_h^e\left(\boldsymbol{x}\right)=\sum_{p=1}^{N_p}q_{h,p}^e l_p\left(\boldsymbol{x}\right),\qquad q_h^e\left(\boldsymbol{x}\right)\in L^2\left(\Omega^e\right), \tag{64}$$

where the nodal Lagrangian basis functions $l_p\left(\boldsymbol{x}_p\right)=1$ and $l_p\left(\boldsymbol{x}_q\right)=0$, $\forall q\neq p$, are defined over the nodal sets shown in Fig. 1. According to Einstein's summation convention, the first term on the left hand side of Eq. (57) can be expanded as,

$$\int_{\Omega_{3d}}\nabla_h v\cdot\left(\mathbf{K}\nabla_h q_h\right)d\boldsymbol{x}=\int_{\Omega_{3d}}\frac{\partial v}{\partial x_i}k_{ij}\frac{\partial q_h}{\partial x_j}d\boldsymbol{x},\quad i,j\in(1,2,3) \tag{65}$$

For the discretization of each term in Eq. (65), the quadrature-free nodal DG method[18,21–23] is used. On each element $\Omega^e\in\Omega_{3d}$, they are discretized as

$$\left(\mathcal{D}_{x_i}^e\right)^T\times\mathcal{M}^e\times\underline{\boldsymbol{k}_{ij}^e}\times\mathcal{D}_{x_j}^e\times\boldsymbol{q}_h^e, \tag{66}$$

where $\boldsymbol{k}_{ij}^e$ is the diagonal matrix holding the discrete nodal values of k_{ij}, $\underline{\boldsymbol{q}_h^e}$ is the vector of discrete nodal values of q_h, $\mathcal{D}_{x_i}^e$ and $\mathcal{M}^e$ are the differentiation matrix and the mass matrix defined over Ω^e, and their components are given as,

$$\mathcal{D}_{x_i}^e\big|_{pq}=\int_{\Omega_e}l_p\left(\boldsymbol{x}\right)\frac{\partial l_q\left(\boldsymbol{x}\right)}{x_i}d\boldsymbol{x},\qquad\mathcal{M}^e\big|_{pq}=\int_{\Omega_e}l_p\left(\boldsymbol{x}\right)l_q\left(\boldsymbol{x}\right)d\boldsymbol{x}. \tag{67}$$

Other terms in Eq. (57) and Eq. (63) are discretized following the same philosophy, and the details are just omitted here.

In addition to the partial derivatives about the non-hydrostatic pressure, both the first-order partial derivative and the mixed partial derivative about σ are also included in Eq. (34), and they are further given by Eqs. (37)–(38) according to Eq. (6). It is noted that only first-order partial derivatives about the bottom topography and water depth are included in Eqs. (37)–(38). These terms are all calculated following the same philosophy as that for the first-order partial derivatives about non-hydrostatic pressure, and the central flux is adopted to specify the unique numerical flux at the elemental boundaries. Following Engsig-Karup et al. [24,25], products of different partial derivatives are evaluated by the direct products of the interpolant functions at interpolation nodes. Although, this approach suffers from aliasing errors, it allows for an efficient way of reconstructing the operators, which is considered to be necessary for the implementation of the method to be relatively simple. Finally, a global linear system for non-hydrostatic pressure is formed and is given as

$$A\boldsymbol{q}=\boldsymbol{b}, \tag{68}$$

where A is the global sparse stiff matrix and $\boldsymbol{b}$ is the right-hand side of the system. System (68) is solved with the direct solver provided by Pardiso [26].

5. Numerical tests

Four numerical tests are conducted in this section. All the tests are conducted on an Intel Xeon E5-2620 processor with 16 GB internal memory. For the first case, we show that the newly derived Poisson equation is better than the original Poisson equation in terms of the convergence property in the framework of the quadrature-free DG method. For the second case, we show that the three-dimensional non-hydrostatic model with the newly derived Poisson-type equation has a smaller numerical error than the original one. For the third case, we show that the three-dimensional non-hydrostatic model with the newly derived Poisson equation can simulate the theoretical case well. For the last case, we show that the developed model can properly simulate combined wave refraction and diffraction.

5.1. Test case with a manufactured solution

For this case, we use the method of manufactured solutions [27] to study the convergence properties of both the newly derived Poisson-type equation and the original equation. The horizontal projection of the horizontal domain is $\Omega_{2d}=[-1,1]\times[-1,1]$, and the bottom topography, the water depth and the non-hydrostatic pressure are given as

$$b\left(x,y\right)=0, \tag{69}$$
$$D\left(x,y\right)=0.04\cos\left(\pi x\right)\cos\left(\pi y\right)+1.0, \tag{70}$$
$$q\left(x,y,\sigma\right)=\sin\left(-\frac{\pi}{2}\sigma\right)\sin\left(\frac{\pi}{2}x\right)\sin\left(\frac{\pi}{2}y\right). \tag{71}$$

These functions are chosen well such that each term on the left-hand side of Eq. (1) and Eq. (34) can be calculated analytically. Following the setup of boundary conditions for the non-hydrostatic model, the Dirichlet boundary condition is imposed at the surface ($\sigma=0$), while the Neumann boundary condition is imposed at the rest of the boundaries. We further substitute the manufactured solution into the left-hand sides of Eq. (1) and Eq. (34) to obtain the right-hand side.

Tests are run with successively refined meshes. For the coarsest mesh, there are 4 uniform elements both in the x and y directions and 2 vertical layers. We refine the mesh up to 4 times and compute the L_2 error of the non-hydrostatic pressure against the analytical solution as follows:

$$L_{2-error}=\frac{1}{\sum_e\int_{\Omega_e}d\boldsymbol{x}}\left(\sum_e\int_{\Omega_e}\left(Q_e^S\left(\boldsymbol{x}\right)-Q_e^{exact}\left(\boldsymbol{x}\right)\right)^2d\boldsymbol{x}\right)^{1/2}, \tag{72}$$

where $Q_e^S\left(\mathbf{x}\right)$ is the numerical result and $Q_e^{exact}\left(\mathbf{x}\right)$ is the analytical solution. To measure the convergence properties of the model, we define the convergence rate (CR) as follows:

$$\mathrm{CR}=\log_2\left(L_{error-2}^m/L_{error-2}^{m-1}\right)/\log_2\left(L^m/L^{m-1}\right), \tag{73}$$

where $L_{error-2}^m$ and $L_{error-2}^{m-1}$ are the numerical errors on two successive refined meshes and L^m and L^{m-1} are the characteristic lengths of the meshes.

The L_2 error and the CR of the original Poisson-type equation and the newly derived equation are listed in Table 1 and Table 2. We find that the model of the original Poisson-type equation converges at order one when the approximation order $N_h=N_v=1$ and approximately converges at order three when $N_h=N_v=2$. However, the model of the

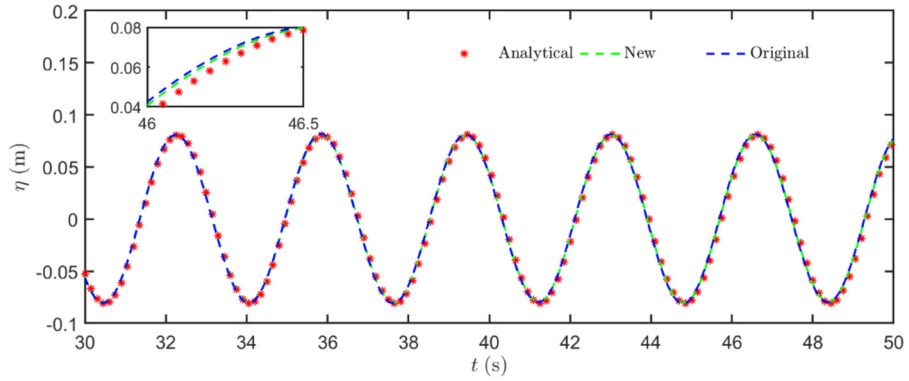

Fig. 2. Comparison of the numerical results (blue dashed line for original Poisson-type equation and green dashed line for newly derived Poisson-type equation) with the analytical solution (red stars) for the time history of water surface elevation at $x = 18.0$.

Table 1
Comparison of the L_2 error and CR between the original and newly derived Poisson equation for approximation order $N_h = N_v = 1$.

Num	N_e	N_L	Original equation		Newly derived equation	
			$L_{2-error}$	CR	$L_{2-error}$	CR
1	16	2	1.75×10^{-2}	\	3.10×10^{-4}	\
2	64	4	8.53×10^{-3}	1.04	8.09×10^{-5}	1.94
3	256	8	4.01×10^{-3}	1.09	2.03×10^{-5}	1.99
4	1024	16	1.91×10^{-3}	1.07	5.09×10^{-6}	2.00

Table 2
Comparison of the L_2 error and CR between the original and newly derived Poisson equation for approximation order $N_h = N_v = 2$.

Num	N_e	N_L	Original equation		Newly derived equation	
			$L_{2-error}$	CR	$L_{2-error}$	CR
1	16	2	1.69×10^{-3}	\	7.25×10^{-6}	\
2	64	4	2.54×10^{-4}	2.73	5.47×10^{-7}	3.73
3	256	8	3.36×10^{-5}	2.92	3.66×10^{-8}	3.90
4	1024	16	4.27×10^{-6}	2.98	2.36×10^{-9}	3.95

new Poisson-type equation converges at the optimal order of two or three when the approximation order N_h and N_v is set to be 1 or 2, respectively. A comparison of the CR indicates that the new Poisson-type equation has better convergence properties than the original equation in the framework of the quadrature-free DG method.

5.2. Standing wave in a closed basin

For the second case, a standing wave in a closed basin is studied. This basin is 20 m long and 1.0 m wide, and the still water depth is $h = 10$ m. This case is widely used for the validation of non-hydrostatic models [2,3]. Initially, all velocity components are set to zero, and the initial water surface elevation is set to

$$\eta = A\cos\left(\frac{\pi x}{10}\right) 0 \le x \le 20, \tag{74}$$

where the wave amplitude is $A = 0.1$ m. The wavelength of the standing wave is $L = 20$ m. According to the linear dispersion relation,

$$\sigma^2 = gk\tanh(kh), \tag{75}$$

with $\sigma = 2\pi/T$ and $k = 2\pi/L$, we can obtain a period of the wave of $T = 3.59$ s. The linearized analytical solution for this standing wave is

$$\eta = a\cos(kx)\cos(\sigma t). \tag{76}$$

For this case, the uniform elemental size is 0.5 m in both the x and y directions, and the number of vertical layers is $N_L = 1$. The horizontal approximation order is $N_h = 1$, and the vertical approximation order is $N_z = 3$. The whole simulation lasts for 50 s, and the time step is taken as a constant value, $\Delta t = 0.005$ s.

In Fig. 2, we compare the numerical results with the analytical solution for the time history of the water surface elevation at $x = 18.0$. It can be found that a small phase error exists for the non-hydrostatic model with the different Poisson-type equations adopted. For a better view, a magnified version is also included in Fig. 2. It is clear that the non-hydrostatic model with the newly derived Poisson-type equation approximates the analytical solution better than the non-hydrostatic model with the original Poisson-type equation. To quantitatively measure this difference, we define the root mean square error (RMSE) as follows:

$$\mathrm{RMSE} = \sqrt{\frac{\sum_{j=1}^{N_T}\left(\eta_{a,j} - \eta_j\right)^2}{N_T}}, \tag{77}$$

where N_T is the total time steps, η_j is the numerical result at step j and $\eta_{a,j}$ is the analytical solution at the same step. The results show that the RMSE for the non-hydrostatic model with the newly derived Poisson-type equation is 2.67e−3, while 3.40e−3 for the model with the original Poisson-type equation. This indicates that the non-hydrostatic model with the newly derived Poisson equation has a smaller numerical error than that with the original Poisson equation.

5.3. Solitary wave propagation in a channel

The solitary wave is an important feature in realistic ocean dynamics and has been widely used for the validation of non-hydrostatic models [2,3,13,28,29]. The solitary wave is also simulated in this study to show the low dissipation of the model. Owing to the balance between nonlinearity and dispersion, the computed solitary wave should maintain its initial profile propagating through a channel with both the friction and viscosity ignored. The channel is 100 m long and 1.0 m wide, and the still water depth is $h = 1.0$ m. A solitary wave with the wave height to the still water depth ratio $\varepsilon = H/h = 0.2$ is appointed according to the third-order analytical solution derived by Fenton [30]. The uniform mesh size is $1/3$ m in both the x and y directions, and the number of vertical layers is $N_L = 1$. The horizontal approximation order is $N_h = 1$, and the vertical approximation order is $N_z = 3$. The whole simulation lasts for 20 s.

During the simulation, the solitary wave moves approximately with the wave speed $c = \sqrt{gh(1+\varepsilon)} = 3.43$ m/s from left to right. In Fig. 3, we compare the numerical results with the analytical solutions for horizontal velocity u, surface elevation η, vertical velocity w and total pressure p at the half water depth. Except for the small undulation in the tail caused by the inconsistency between the initial condition and the governing equations, the numerical solutions generally match well with the analytical solutions.

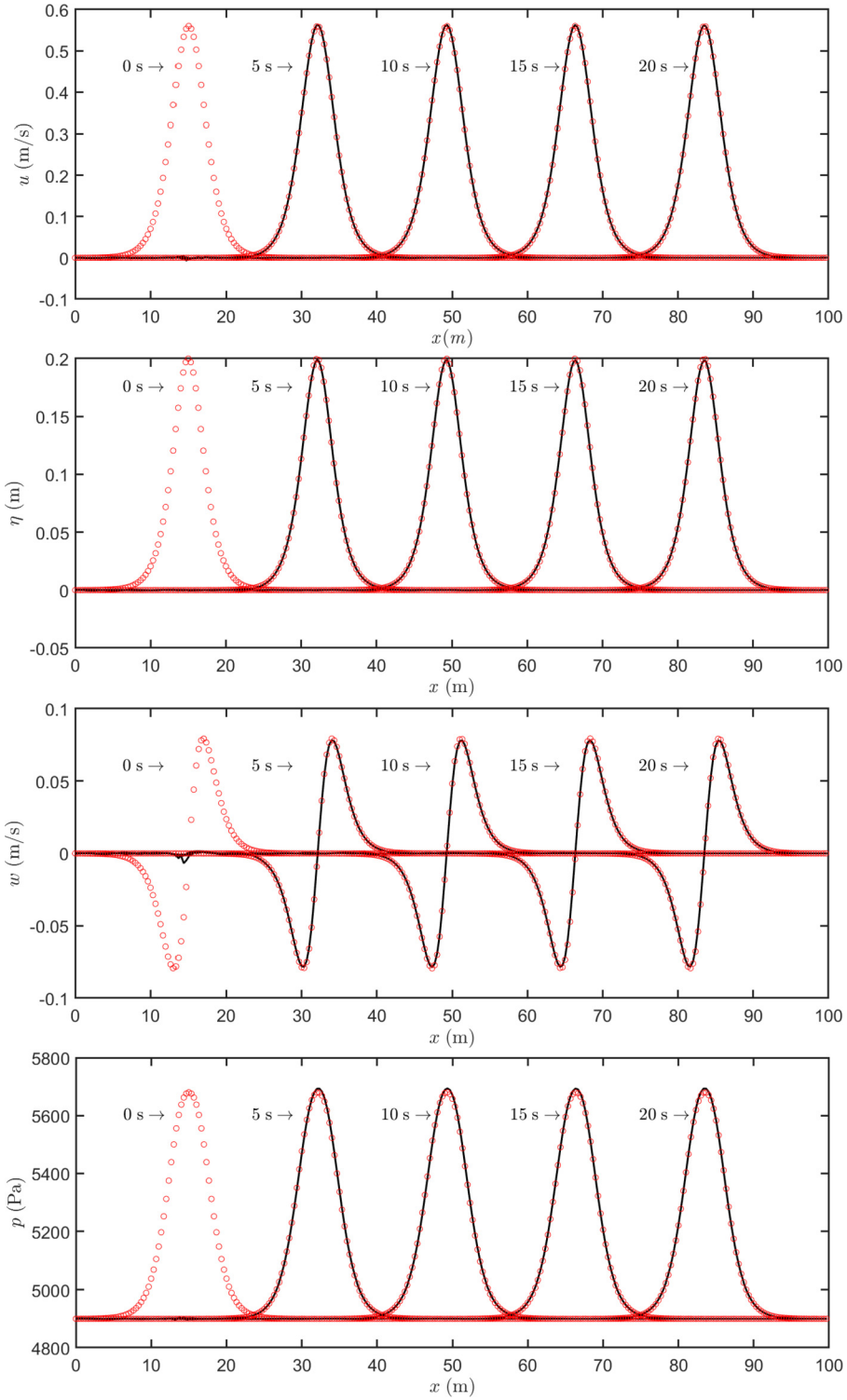

Fig. 3. Comparison of the numerical results (black line) with the analytical solutions (red circle) for horizontal velocity u, surface elevation η, vertical velocity w and total pressure p at time points 5 s, 10 s, 15 s and 20 s.

To further measure the dissipation of the developed non-hydrostatic model with the newly derived Poisson equation adopted, we define the relative error (RE) as follows:

$$\mathrm{RE} = \left(\phi_{comp} - \phi_{ana}\right)/\phi_{ana}, \tag{78}$$

where ϕ_{comp} is the maximum value of the numerical result and ϕ_{ana} is that of the analytical solution. In Fig. 4, we give the time history of the RE for the maximum surface elevation $\eta_{\max}$, the maximum horizontal velocity $u_{\max}$, the maximum vertical velocity $w_{\max}$ and the maximum total pressure $p_{\max}$. From Fig. 4, we can infer that there is a redistribution of the solution for prognostic variables η, u and w since the initial condition is not compatible with the governing equations, and this redistribution finishes at approximately 1.75 s, after which the distribution of the prognostic variables becomes relatively stable. During the whole simulation, the RE of the maximum value for all the prognostic variables is controlled well, and the maximum absolute value is

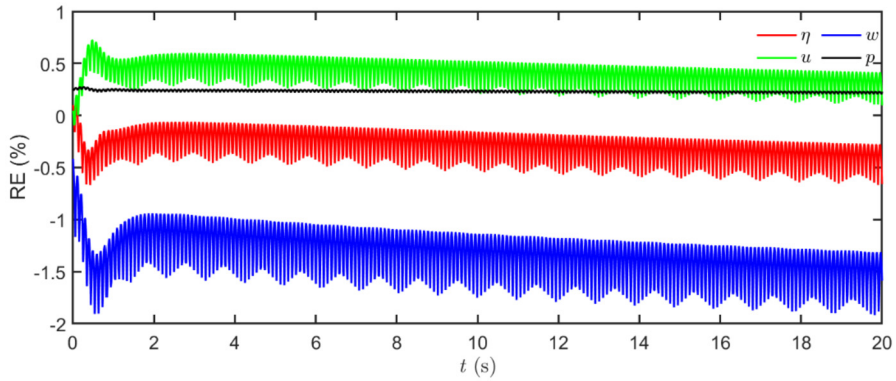

Fig. 4. Time history of the RE for the maximum surface elevation $\eta_{\max}$, the maximum horizontal velocity $u_{\max}$, the maximum vertical velocity $w_{\max}$ and the maximum total pressure $p_{\max}$.

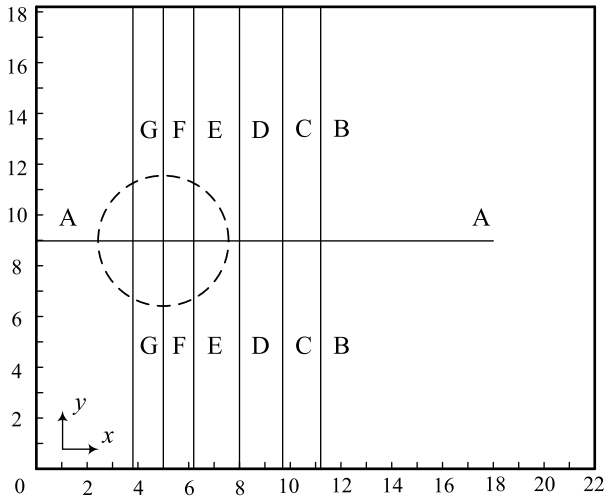

Fig. 5. Experimental setup of wave transformation over a circular shoal.

less than 2%. For the diagnostic variable, i.e., the total pressure p, the RE of the maximum value is approximately 0.25%. We note that the RE oscillates around a given value since the mesh resolution is finite.

5.4. Wave transformation over a circular shoal

For the last case, the wave transformation over a circular shoal is modelled to validate the capability of the model for the simulation of complex wave transformation in the combined wave refraction and diffraction. The experimental setup of this case is provided by Chawla [31] and is shown in Fig. 5. This wave basin is 22 m long in x direction and 18.2 m wide in y direction, and a circular shoal is placed on an otherwise flat bottom in the basin. The centre of the shoal is located at point (5.0, 8.98), and the perimeter of the shoal is defined as

$$(x-5)^2+(y-8.98)^2=2.57^2. \tag{79}$$

The water depth over the submerged shoal is given by

$$D=D_0+8.73-\sqrt{82.81-(x-5)^2-(y-8.98)^2}, \tag{80}$$

with $D_0=0.45$ the constant water depth of the basin.

For the numerical simulation, the incident wave with height $H_0=0.0118$ m and wave period $T=1$ s are imposed at the left boundary corresponding to $x=0$ m. To minimize wave reflection, a sponge layer of length 4 m is deployed at the right side of the wave basin. The other two lateral walls are treated as reflective boundaries. The approximation order is $N_h=1$ in horizontal direction and $N_z=3$ in vertical direction. We choose a uniform element size of 0.075 m in x direction and 0.15 m in y direction, only one layer is adopted in vertical direction, and the whole computational domain consists of 35453 quadrangular prisms. The whole simulation lasts for 40 s.

The three-dimensional free surface at $t=40$ s is shown in Fig. 6. Due to the uneven topography, wave diffraction and wave refraction are formed on the leeward side of the shoal. To provide the details of the simulated results, we also present a comparison of the measured relative wave height and the simulated relative wave height at the seven cross sections shown in Fig. 7. The simulated relative wave height is defined as H_1/H_0, where H_1 is the simulated wave height and is obtained by taking the difference between the maximum and the minimum free-surface elevation over the last 10 periods during which the wave form is steady.

From Fig. 7, a close agreement between the numerical results and the experimental data of Chawla [31] is observed, and the relative wave height reaches the value of 2.7, as shown in Fig. 7a. The close agreement between the numerical results and the measured data observed along cross sections at $x=3.8$ m, $x=5.0$ m, $x=6.2$ m, $x=8.0$ m, $x=9.7$ m and $x=11.2$ m (Fig. 7b–g) indicates that the combined refraction and diffraction effects are captured successfully by the developed model. It's also noted that the shoal centre is located at the $y=8.98$ m (the width of the basin is 18.2 m), which is slightly closer to one of the side walls ($y=0$ m). Therefore, the distribution of wave height in the y direction is not symmetric, and this can be observed in Fig. 7b–g.

6. Conclusion

In this study, a new Poisson-type equation for the non-hydrostatic pressure in the terrain-following σ coordinate is proposed. The resultant Poisson-type equation consists of a standard elliptic operator and other first-order operators for non-hydrostatic pressure.

Compared with the original Poisson-type equation, the treatment of the boundary condition at the lateral boundary can be simplified. The test case of the manufactured solution indicates that the newly derived Poisson-type equation has better convergence properties than the original equation in the framework of the quadrature-free nodal DG method and that it can achieve the optimal CR when the approximation order is set to 1 or 2. Additionally, the test case of the standing wave indicates that the non-hydrostatic model with the newly derived Poisson-type equation has a smaller numerical error than that with the original equation. For the time history of the surface elevation for a given point, the RMSE is 2.67e−3 for the non-hydrostatic model with the newly derived Poisson-type equation, while it is 3.40e−3 for the non-hydrostatic model with the original equation. Test case of the solitary wave shows that the absolute RE for the maximum surface elevation $\eta_{\max}$, the maximum horizontal velocity $u_{\max}$, the maximum vertical velocity $w_{\max}$ and the maximum total pressure $p_{\max}$ are less than 2%, indicating the small dissipative nature of the developed model. In addition, transformation

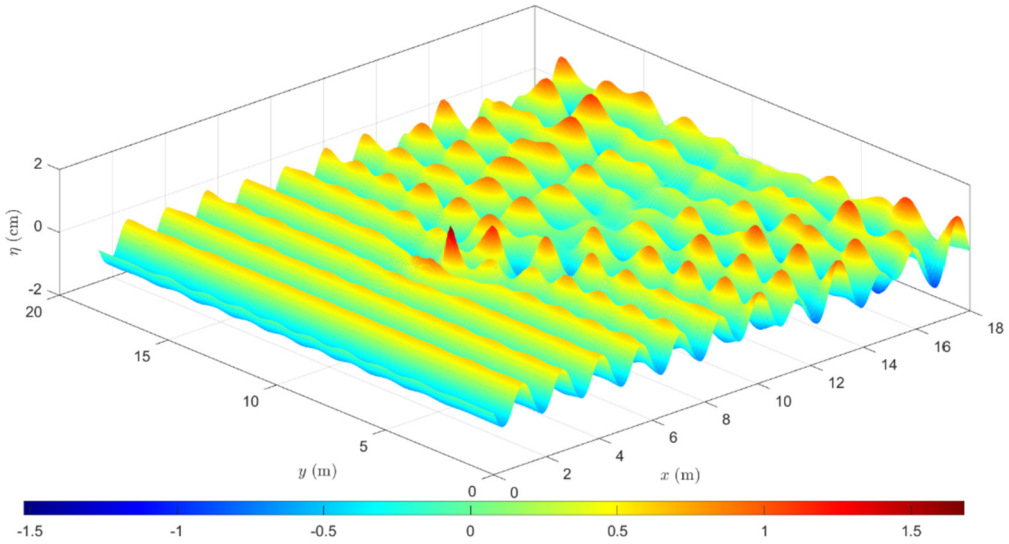

Fig. 6. 3-D presentation of the free-surface elevation for the case of wave transformation over a circular shoal at $t = 40$ s.

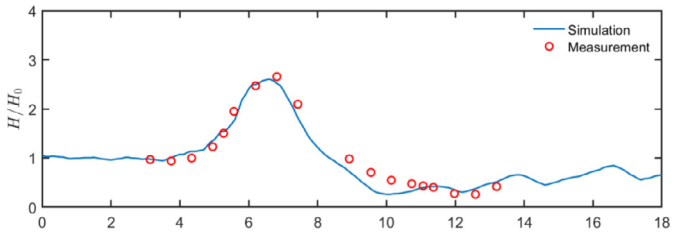

(a) Section A-A ($y = 8.98$ m)

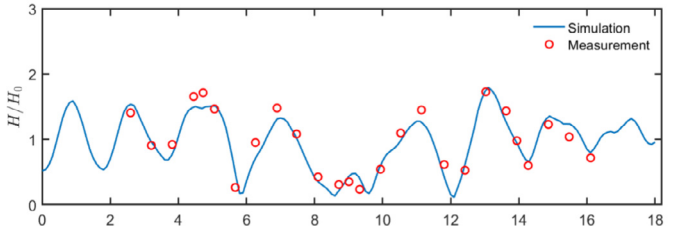

(b) Section B-B ($x = 11.2$ m)

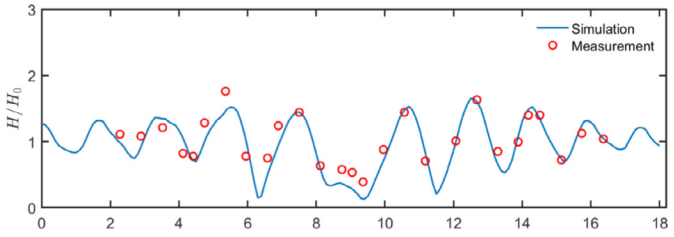

(c) Section C-C ($x = 9.7$ m)

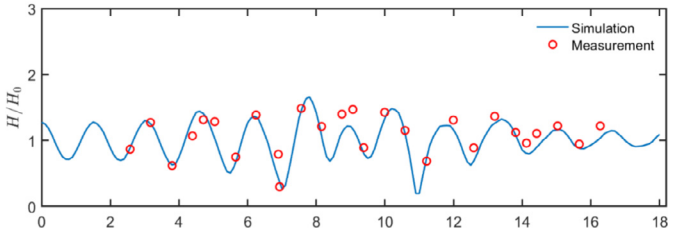

(d) Section D-D ($x = 8.0$ m)

Fig. 7. Comparison of the relative wave height calculated by the developed model with laboratory measurement.

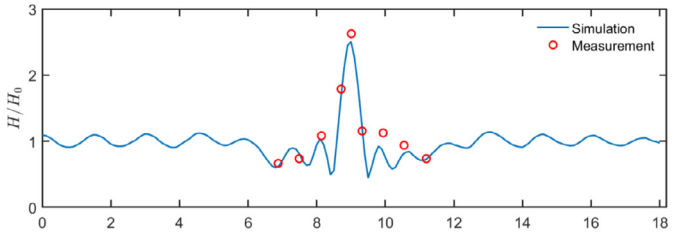

(e) Section E-E ($x = 6.2$ m)

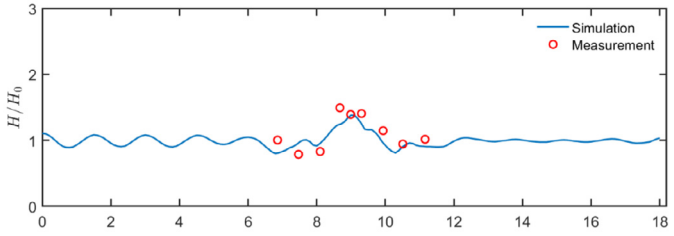

(f) Section F-F ($x = 5.0$ m)

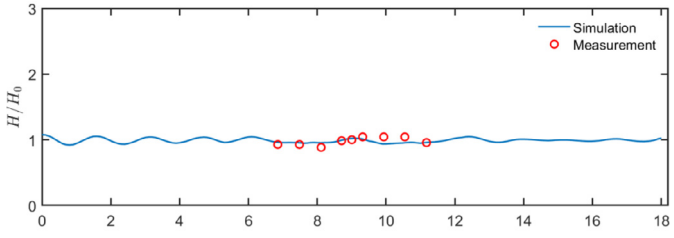

(g) Section G-G ($x = 3.8$ m)

Fig. 7. (*continued*)

of wave over a circular shoal indicates that the developed model can properly simulate combined wave refraction and diffraction.

More details about the numerical implementation and results about the non-hydrostatic model will be given in a forthcoming paper.

Data availability

No data was used for the research described in the article.

Acknowledgements

This work was financially supported by the National Key Research and Development Program of China (Grant No. 2021YFB2601100), the Joint Funds of the National Natural Science Foundation of China (Grant No. U1906231), Natural Science Foundation of Tianjin (Grant No. 19JCZDJC40200), Special Key Program for Technological Innovation and Application Development in Chongqing (Grant No. CSTB2022TIAD-KPX0198), the Joint Key Program of Science and Technology Project between Chongqing Science and Technology Bureau and Chongqing Water Resources Bureau (Grant No. CQSLK-2022001), and Major Science and Technology Program of the Ministry of Water Resources (Grant No. SKS-2022076).

References

[1] C. Ai, W. Ding, S. Jin, A general boundary-fitted 3D non-hydrostatic model for nonlinear focusing wave groups, Ocean Eng. 89 (2014) 134–145.
[2] G. Ma, F. Shi, J.T. Kirby, Shock-capturing non-hydrostatic model for fully dispersive surface wave processes, Ocean Model. 43–44 (2012) 22–35.
[3] G. Stelling, M. Zijlema, An accurate and efficient finite-difference algorithm for non-hydrostatic free-surface flow with application to wave propagation, Int. J. Numer. Methods Fluids 43 (2003) 1–23.
[4] M. Zijlema, G.S. Stelling, Further experiences with computing non-hydrostatic free-surface flows involving water waves, Int. J. Numer. Methods Fluids 48 (2005) 169–197.
[5] W. Pan, S.C. Kramer, M.D. Piggott, A σ-coordinate non-hydrostatic discontinuous finite element coastal ocean model, Ocean Model. 157 (2021) 101732.
[6] I. Magdalena, A dispersive numerical model for the formation of undular bores generated by tsunami wave fission, East Asian J. Appl. Math. 7 (2018) 767–784.
[7] I. Magdalena, N. Erwina, An efficient two-layer non-hydrostatic model for investigating wave run-up phenomena, Computation 8 (2020).
[8] S.R. Pudjaprasetya, I. Magdalena, S.S. Tjandra, A nonhydrostatic two-layer staggered scheme for transient waves due to anti-symmetric seabed thrust, J. Earthq. Tsunami 11 (2017) 1740002.
[9] P. Higuera, J.L. Lara, I.J. Losada, Realistic wave generation and active wave absorption for Navier–Stokes models: application to OpenFOAM®, Coast. Eng. 71 (2013) 102–118.
[10] H.C. Chen, Y. Kai, CFD simulations of wave–current-body interactions including greenwater and wet deck slamming, Comput. Fluids 38 (2009) 970–980.
[11] F.H. Harlow, J.E. Welch, Numerical calculation of time-dependent viscous incompressible flow of fluid with free surface, Phys. Fluids 8 (1965) 2182–2189.
[12] N. Fehn, W.A. Wall, M. Kronbichler, On the stability of projection methods for the incompressible Navier-Stokes equations based on high-order discontinuous Galerkin discretizations, J. Comput. Phys. 351 (2017) 392–421.
[13] Z. Lai, C. Chen, G.W. Cowles, R.C. Beardsley, A non-hydrostatic version of FVCOM, part I: validation experiments, J. Geophys. Res., Oceans 115 (2010).
[14] P. Lin, C.W. Li, A σ-coordinate three-dimensional numerical model for surface wave propagation, Int. J. Numer. Methods Fluids 38 (2010) 1045–1068.
[15] B. Krank, N. Fehn, W.A. Wall, M. Kronbichler, A high-order semi-explicit discontinuous Galerkin solver for 3D incompressible flow with application to DNS and LES of turbulent channel flow, J. Comput. Phys. 348 (2017) 634–659.
[16] N. Fehn, W.A. Wall, M. Kronbichler, Robust and efficient discontinuous Galerkin methods for under-resolved turbulent incompressible flows, J. Comput. Phys. 372 (2018) 667–693.
[17] N.A. Phillips, A coordinate system having some special advantages for numerical forecasting, J. Atmos. Sci. 14 (1957) 184–185.
[18] J.S. Hesthaven, T. Warburton, Nodal Discontinuous Galerkin Methods. Algorithms, Analysis, and Applications, Springer, New York, 2008.
[19] D. Pietro, A. Ern, Mathematical Aspects of Discontinuous Galerkin Methods, Springer-Verlag, Berlin, 2012.
[20] A. Ern, A.F. Stephansen, P. Zunino, A discontinuous Galerkin method with weighted averages for advection–diffusion equations with locally small and anisotropic diffusivity, IMA J. Numer. Anal. 29 (2008) 235–256.
[21] L. Li, Q. Zhang, A new vertex-based limiting approach for nodal discontinuous Galerkin methods on arbitrary unstructured meshes, Comput. Fluids 159 (2017) 316–326.
[22] L. Li, Q. Zhang, Development of an efficient wetting and drying treatment for shallow-water modeling using the quadrature-free Runge-Kutta discontinuous Galerkin method, Int. J. Numer. Methods Fluids 93 (2020) 314–338.
[23] G. Ran, Q. Zhang, L. Li, A depth-integrated non-hydrostatic model for nearshore wave modelling based on the discontinuous Galerkin method, Ocean Eng. 232 (2021) 108661.
[24] A.P. Engsig-Karup, J.S. Hesthaven, H.B. Bingham, P.A. Madsen, Nodal DG-FEM solution of high-order Boussinesq-type equations, J. Eng. Math. 56 (2006) 351–370.
[25] A.P. Engsig-Karup, J.S. Hesthaven, H.B. Bingham, T. Warburton, DG-FEM solution for nonlinear wave-structure interaction using Boussinesq-type equations, Coast. Eng. 55 (2008) 197–208.
[26] C.L. Alappat, G. Hager, O. Schenk, J. Thies, A. Basermann, A. Bischop, H. Fehske, G. Wellein, A recursive algebraic coloring technique for hardware-efficient symmetric sparse matrix-vector multiplication, ACM Trans. Math. Softw. 7 (2020).
[27] K. Salari, P. Knupp, Code Verification by the Method of Manufactured Solutions, Sandia National Laboratories, 2000.
[28] D.Y. Choi, C.H. Wu, A new efficient 3D non-hydrostatic free-surface flow model for simulating water wave motions, Ocean Eng. 33 (2006) 587–609.
[29] M.M. Namin, B. Lin, R.A. Falconer, An implicit numerical algorithm for solving non-hydrostatic free-surface flow problems, Int. J. Numer. Methods Fluids 35 (2015) 341–356.
[30] J.J. Fenton, A ninth-order solution for the solitary wave, J. Fluid Mech. 53 (1972) 257–271.
[31] A. Chawla, Wave Transformation over a Submerged Shoal, University of Delaware, 1995.